nature chemistry

SUPPLEMENTARY INFORMATION

https://doi.org/10.1038/s41557-018-0066-z

In the format provided by the authors and unedited.

Solvents can control solute molecular identity

Devon. R. Widmer* and Benjamin J. Schwartz*

Department of Chemistry & Biochemistry, University of California, Los Angeles, Los Angeles, CA, USA. *e-mail: widmer@chem.ucla.edu; schwartz@chem.ucla.edu

Supplementary Information to "Solvents can control solute molecular identity"

Devon. R. Widmer and Benjamin J. Schwartz*

Department of Chemistry & Biochemistry,

University of California, Los Angeles,

Los Angeles, CA 90095-1569 USA

Contents

Simulation Details

Mixed Quantum/Classical Model

In addition to classical solvent molecules, our mixed quantum/classical (MQC) molecular dynamics (MD) simulations, which were performed in the microcanonical ensemble, consisted of two classical Na^+ cations and two fully quantum mechanical electrons. For simulations in liquid Ar, we used a simulation cell of side length 43.8 Å and 1600 solvent molecules, while our simulations in liquid THF used a simulation cell of side length 32.5 Å and 254 solvent molecules. The choice of cell size reproduced appropriate solvent densities at the simulation temperatures (1.26 g/mL at 120 ± 2 K for Ar simulations and 0.89 g/mL at 298 ± 6 K for THF simulations). The THF molecules were treated as rigid, planar five-membered rings following the work of Chandrasekar and Jorgensen.[1] The rigid planarity of the molecules was enforced using the RATTLE algorithm, as in our previous MQC MD work in this solvent.[2] Periodic boundary conditions were implemented with minimum image convention[3] and all interactions were tapered smoothly to zero at 16 Å over a 2 Å range with a center of mass-based switching function due to Steinhauser.[4]

All interactions were taken to be pair-wise additive. Thus, the full Hamiltonian of the system is $\hat{H} = H^{\mathrm{cl}} + \hat{H}^{\mathrm{qm}}$. In atomic units, the classical portion of the Hamiltonian is given by

$$H^{\mathrm{cl}} = \frac{1}{2} m_{\mathrm{Na}^+} \sum_{i=1}^{2} v_{\mathrm{Na}^+{}_i}^2 + \frac{1}{2} m_{\mathrm{solv}} \sum_{i=1}^{n_{\mathrm{solv}}} v_{\mathrm{solv}_i}^2 + U^{\mathrm{Na}^+-\mathrm{Na}^+}(|\boldsymbol{R}_{\mathrm{Na}^+{}_1} - \boldsymbol{R}_{\mathrm{Na}^+{}_2}|) + \sum_{i=1}^{n_{\mathrm{solv}}} \sum_{j>i}^{n_{\mathrm{solv}}} U^{\mathrm{solv}-\mathrm{solv}}(|\boldsymbol{R}_{\mathrm{solv}_i} - \boldsymbol{R}_{\mathrm{solv}_j}|) + \sum_{i=1}^{2} \sum_{j=1}^{n_{\mathrm{solv}}} U^{\mathrm{Na}^+-\mathrm{solv}}(|\boldsymbol{R}_{\mathrm{Na}^+{}_i} - \boldsymbol{R}_{\mathrm{solv}_j}|) \quad (1)$$

where v_{χ_i} is the velocity of the i^{th} sodium (χ = Na^+) or solvent molecule (χ = solv) at position $\boldsymbol{R}_{\chi_i}$ and mass m_χ. $U^{\chi-\gamma}$ is a classical potential between atom types χ and γ (χ, γ = Na^+ or solv).

The quantum Hamiltonian is given by

$$\hat{H}^{\mathrm{qm}} = \sum_{i=1}^{2} \frac{\hat{\boldsymbol{p}}_i^2}{2} + \sum_{i=1}^{2} \sum_{j=1}^{2} V^{\mathrm{Na}^+}(|\boldsymbol{R}_{\mathrm{Na}^+{}_j} - \hat{\boldsymbol{r}}_i|) + \sum_{i=1}^{2} \sum_{j=1}^{n_{\mathrm{solv}}} V^{\mathrm{solv}}(|\boldsymbol{R}_{\mathrm{solv}_j} - \hat{\boldsymbol{r}}_i|) + \hat{r}_{12}^{-1} \quad (2)$$

where $\hat{\boldsymbol{p}}_i$ and $\hat{\boldsymbol{r}}_i$ are the momentum and position operators for electron i, respectively, V^{χ} is the pseudopotential representing the interaction between an electron and atom type χ, and $\hat{r}_{12}^{-1}$ is the Coulomb operator for the two valence electrons.

We modeled the classical interactions between the two Na^+ cations through a point-charge Coulomb potential, $U^{Na^+-Na^+}(R) = 1/R$, since the short-range repulsion between the cores is negligible around the internuclear separation of Na_2. The Na^+-Ar interaction was taken from a fit to the *ab initio* calculations of Ahmadi, Almlöf, and Røeggen:[5]

$$U^{Na^+-Ar}(R) = \frac{a_1 \exp(-a_2 R)}{R} - \frac{2}{1 + a_1 \exp(a_3/R)} \left(\frac{C_6}{R^6} + \frac{C_8}{R^8} \right) \tag{3}$$

where $a_1 = 242.32$ Hartree, $a_2 = 1.67$ bohr^{-1}, $a_3 = 5.6$ bohr, $C_6 = 255$ bohr^5, and $C_8 = 4410$ bohr^7. Following Gervais et al,[6] we have subtracted the charge-dipole term, which goes as $-0.5\alpha_{Ar}/R^4$, where α_{Ar} is the dipole polarizability of Ar, since Ar is interacting with a net neutral Na_2 species. All other classical interactions were modeled with Lennard-Jones potentials:[3]

$$u_{ij}(r_{ij}) = \frac{1}{4\pi\epsilon_0} \frac{q_i q_j}{r_{ij}} + 4\epsilon_{ij} \left[\left(\frac{\sigma_{ij}}{r_{ij}} \right)^{12} - \left(\frac{\sigma_{ij}}{r_{ij}} \right)^{6} \right] \tag{4}$$

where r_{ij} is the distance between the i^{th} and j^{th} solvent/Na^+ site, q_i is the charge on the i^{th} site, ϵ_{ij} is the potential well depth, and σ_{ij} is the finite distance at which the inter-particle potential is zero. The Lennard-Jones parameters used in this study are listed in Supplementary Table 1. The standard Lorentz-Berthelot combining rules were used to calculate the solute-solvent site and solvent site-solvent site interactions in THF.[3]

	σ (Å)	ϵ (kJ/mol)	q (e)
Argon	3.405	0.996	0.0
THF-oxygen	3.0	0.71	–0.5
THF-α-methyl	3.8	0.49	+0.25
THF-β-methyl	3.905	0.49	0.0
Na^+	1.67	22.07	+1.0

Supplementary Table 1: Lennard-Jones and Coulomb Potential Parameters for the Solute-Solvent Systems Studied in This Work.

Interactions between the classical particles and the quantum mechanical electrons were accounted for using Phillips Kleinman (PK) pseudopotentials[7] modified with polarization potentials to correct for the frozen-core approximation implicit in PK formalism.[8–10] For the electron-Ar interaction, $V^{e^- - \mathrm{Ar}}$, we used a modified version of the pseudopotential developed by Gervais *et al*,[6] described in detail in our previous work.[11] For $V^{e^- - \mathrm{Na}^+}$ and $V^{e^- - \mathrm{THF}}$, we used rigorously-derived psedopotentials previously developed by our group, the details of which can be found in Refs. 12 and 10, respectively. The final pseudopotential fits are presented here in Supplementary Tables 2 and 3.

i	c_i (a.u.)	α_i (a.u.)
1	-0.103 055 903	0.189 844 564
2	0.436 627 83	0.069 933
3	0.541 733 81	0.032 893
4	0.134 538 22	0.016 122

Supplementary Table 2: Parameters used in the construction of the sodium-electron pseudopotential, $\phi(r) = \sum_{i=1}^{4} c_i e^{-\alpha_i r^2}$**.** Further details of the sodium-electron pseupotential can be found in Ref 12.

$$U_{fit}(\mathbf{r}) = \begin{cases} & U_o & + & U_{c\alpha 1} & + & U_{c\alpha 2} & + & U_{c\beta 1} & + & U_{c\beta 2} \\ + & U_{h\alpha 1} & + & U_{h\alpha 2} & + & U_{h\alpha 3} & + & U_{h\alpha 4} & + & U_{h\beta 1} \\ + & U_{h\beta 2} & + & U_{h\beta 3} & + & U_{h\beta 4} & + & U_{ao} & + & U_{ao} \\ + & U_{ac} & + & U_{ac} & + & U_{aa} & + & U_{af} & & \end{cases}$$

$$U_o(\mathbf{r}-\mathbf{r_o}) = \begin{array}{rl} & \left(o_1(x-x_o)^4 + o_2(y-y_o)^4 + o_3(z-z_o)^4 - o_4\right) \\ \times & exp\left(-\left[o_5(x-x_o)^2 + o_6((y-y_o)^2 + (z-z_o)^2)\right]\right) \\ + & o_7 \frac{e^{-o_8(\mathbf{r}-\mathbf{r_o})^2}}{|\mathbf{r}-\mathbf{r_o}|} \end{array}$$

$o_1 = 2.8926$	$o_2 = 0.1017$	$o_3 = 1.9379$	$o_4 = 4.1887$
$o_5 = 1.0552$	$o_6 = 1.2853$	$o_7 = 9.4147$	$o_8 = 23.4135$

$$U_{c\alpha}(\mathbf{r}-\mathbf{r_{c\alpha}}) = \begin{array}{rl} & c_1^\alpha\left[(y-y_{c\alpha}) + c_2^\alpha(z-z_{c\alpha})\right] \\ \times & exp\left(-\left[c_3^\alpha(x-x_{c\alpha})^2 + c_4^\alpha((y-y_{c\alpha})^2 + (z-z_{c\alpha})^2)\right]\right) \\ - & c_5^\alpha \frac{1}{|\mathbf{r}-\mathbf{r}_{c\alpha}|} + c_6^\alpha exp\left[-c_7^\alpha(\mathbf{r}-\mathbf{r}_{c_\alpha})^4\right] \end{array}$$

$c_1^\alpha = 62.6462$	$c_2^\alpha = 0.1426$	$c_3^\alpha = 7.9044$	$c_4^\alpha = 7.9516$
$c_5^\alpha = 0.3147$	$c_6^\alpha = 6.3821$	$c_7^\alpha = 34.2773$	

$$U_{c\beta}(\mathbf{r}-\mathbf{r_{c\beta}}) = \begin{array}{rl} & c_1^\beta\left[(y-y_{c\beta}) + c_2^\beta(z-z_{c\beta})\right] \\ \times & exp\left[-\left(c_3^\beta(x-x_{c\beta})^2 + c_4^\beta((y-y_{c\beta})^2 + (z-z_{c\beta})^2)\right)\right] \\ - & c_5^\beta \frac{1}{|\mathbf{r}-\mathbf{r}_{c\beta}|} + c_6^\beta e^{-c_7^\beta(\mathbf{r}-\mathbf{r}_{c\beta})^4} \end{array}$$

$c_1^\beta = 13.3107$	$c_2^\beta = 1.3455$	$c_3^\beta = 5.3624$	$c_4^\beta = 4.4085$
$c_5^\beta = 0.3033$	$c_6^\beta = 1.4495$	$c_7^\beta = 7.8897$	

$$U_{h\alpha}(\mathbf{r}-\mathbf{r_{h\alpha}}) = -h_1^\alpha \frac{exp\left[-h_2^\alpha(\mathbf{r}-\mathbf{r}_{h\alpha})^2\right]}{|\mathbf{r}-\mathbf{r}_{h\alpha}|} + h_3^\alpha exp\left[-h_4^\alpha(\mathbf{r}-\mathbf{r}_{h\alpha})^2\right]$$

$h_1^\alpha = 0.8357$	$h_2^\alpha = 0.8769$	$h_3^\alpha = 0.2657$	$h_4^\alpha = 0.0852$

$$U_{h\beta}(\mathbf{r}-\mathbf{r_{h\beta}}) = -h_1^\beta \frac{exp\left[-h_2^\beta(\mathbf{r}-\mathbf{r}_{h\beta})^2\right]}{|\mathbf{r}-\mathbf{r}_{h\beta}|} + h_3^\beta exp\left[-h_4^\beta(\mathbf{r}-\mathbf{r}_{h\beta})^2\right]$$

$h_1^\beta = 0.7861$	$h_2^\beta = 0.9584$	$h_3^\beta = 0.1362$	$h_4^\beta = 0.0359$

$$U_{ao}(\mathbf{r}-\mathbf{r_{ao}}) = a_1^o exp\left[-\left(a_2^o(x-x_{ao})^2 + a_3^o(y-y_{ao})^2 + a_4^o(z-z_{ao})^2\right)\right]$$

$a_1^o = 2.7673$	$a_2^o = 1.0552$	$a_3^o = 0.5211$	$a_4^o = 0.7436$

$$U_{ac}(\mathbf{r}-\mathbf{r_{ac}}) = a_1^c exp\left[-\left(a_2^c(x-x_{ac})^2 + a_3^c((y-y_{ac})^2 + (z-z_{ac})^2)\right)\right]$$

$a_1^c = 0.9996$	$a_2^c = 0.6810$	$a_3^c = 0.3058$	

$$U_{aa}(\mathbf{r}-\mathbf{r_{aa}}) = \begin{array}{rl} & a_1^a exp\left[-\left(a_2^a(x-x_{aa})^2 + a_3^a((y-y_{aa})^2 + (z-z_{aa})^2)\right)\right] \\ - & a_4^a exp\left[-\left(a_5^a(x-x_{aa})^2 + a_6^a((y-y_{aa})^2 + (z-z_{aa})^2)\right)\right] \end{array}$$

$a_1^a = 11.7043$	$a_2^a = 0.5978$	$a_3^a = 0.1703$	
$a_4^a = 10.7099$	$a_5^a = 0.5994$	$a_6^a = 0.1597$	

$$U_{af}(\mathbf{r}-\mathbf{r_{af}}) = a_1^f exp\left[-\left(a_2^f(x-x_{af})^2 + a_3^f(y-y_{af})^2 + a_4^f(z-z_{af})^2\right)\right]$$

$a_1^f = 0.4472$	$a_2^f = 0.0443$	$a_3^f = 0.0379$	$a_3^f = 0.2579$

Supplementary Table 3: Functional Form and Parameters of the Fit to the Exact e^-–THF Effective Potential. The 47-parameter fit has functional contributions centered on 19 different sites. The functional and parameter notations are explained in Ref 10. For the parameters given here, the distances are in Bohr radii and the energies are in Hartrees.

Two-Electron Fourier Grid Method for Solving for the Valence Electrons' Wave function

The details of our two-electron Fourier grid (2EFG) method for solving for the valence electrons' wave function are described extensively in our previous work,[13] but are briefly outlined here for completeness. In our 2EFG method, the valence electrons' wave function is expanded on a six-dimensional real-space grid according to

$$|\Psi\rangle = \sum_{i=1}^{N^3} \sum_{j=1}^{N^3} \Psi_{i,j} \, |\boldsymbol{r}_i \boldsymbol{r}_j\rangle \tag{5}$$

where $|\boldsymbol{r}_i \boldsymbol{r}_j\rangle$ is the basis point of the six-dimensional regular, real-space grid at 6-dimensional position $(\boldsymbol{r}_i, \boldsymbol{r}_j)$, N is the number of grid points in each dimension, and $\Psi_{i,j}$ are the real-valued expansion coefficients in this basis. We enforce spin-singlet symmetry in the expansion coefficients by restricting $\Psi_{i,j} = \Psi_{j,i}$. Constructing the basis in this manner is advantageous because all of the various potential energy operators have a diagonal matrix representation, including the electron–electron Coulomb operator. Furthermore, transforming the real-space wave function to reciprocal-space through fast Fourier transforms also gives the kinetic energy operator a diagonal matrix representation, allowing for rapid construction of the quantum Hamiltonian operator matrix.

MQC Simulations of Na_2 in the Condensed Phase

For simulations in liquid Ar, we used a basis of 16×16×16 grid points distributed over a cubic box with 14 Å sides for the valence electrons, and for simulations in liquid THF, we used a basis of 20×20×20 grid points distributed over a cubic box with 17.5 Å sides, giving a consistent grid spacing of 0.875 Å. These dimensions were chosen to keep the basis set as small as possible for each system while still capturing the spatial extent of electronic wave function, which was larger in THF than Ar. We centered the grid in the middle of the simulation cell and shifted all classical particles relative to the grid every 500 fs to avoid leakage of the wave function off the edges of the grid basis, so that the wave function was always located roughly in the center of the simulation cell. The classical particles were shifted an integer number of grid spaces to avoid discontinuities in the quantum energy that

would prevent total energy of simulation from being conserved.[12] We used the velocity Verlet algorithm[3] to propagate the classical degrees of freedom ($\boldsymbol{v}_{\mathrm{Na^+}_i}$, $\boldsymbol{v}_{\mathrm{solv}_i}$, $\boldsymbol{R}_{\mathrm{Na^+}_i}$, and $\boldsymbol{R}_{\mathrm{solv}_i}$) of the Hamiltonian in Eqs. 1 and 2 in the microcanonical (N, V, E) ensemble. We determined the forces from the sum of the classical-classical and classical-quantum interactions described above. We used the implicit restart Lanczos method to iteratively solve the TISE for the ground state wavefunction at every time step (5 fs in Ar and 4 fs in THF).[14] The quantum forces on the classical particles were then found using the Hellman-Feynman theorem:

$$\boldsymbol{F}_i^Q = -\langle\Psi|\,\boldsymbol{\nabla}_{\boldsymbol{R}_i}\hat{H}\,|\Psi\rangle \tag{6}$$

where, $\boldsymbol{F}_i^Q$ is the quantum force on classical particle i at position $\boldsymbol{R}_i$. Because the wave function is expanded in a basis that does not functionally depend on the position of the classical particles, Eq. 6 is exact (in other words, there are no issues with Pulay forces from the basis functions changing with time).[13]

For Ar, the initial conditions were taken from a classical simulation of LJ Ar at 120 $\pm$2 K, yielding a reduced density of 0.75 that falls within the liquid region of the LJ phase diagram.[15] A solute cavity was carved out by two LJ spheres of an appropriate size to represent the Na_2 solute. The two classical Na^+ cations were then placed in this cavity and particles were shifted such that the Na^+ cations and solute cavity was in the center of the quantum grid. We propagated the MQC system for an equilibration period of 50 ps during which the classical particle velocities were occasionally rescaled to adjust the average temperature to 120 K before a 500-ps production run without velocity rescaling. For THF, we first removed a solvent molecule from an equilibrated snapshot of our previous work with Na^- in THF to make room for the second Na^+ core. We then propagated the MQC system for several hundred picoseconds with velocity rescaling to adjust the average temperature to 298 K before the 500-ps production run.

Analysis Details

Coordination Number Interconversion

We extracted interconversion times between coordination states from our THF simulation trajectory by binning up the times the Na_2 molecule spent in each coordination state before converting to another. From this analysis, we determined conversion times of 32 ± 10 ps and 37 ± 19 ps for the $Na(THF)_3$–$Na(THF)_3$ → $Na(THF)_3$–$Na(THF)_4$ and $Na(THF)_3$–$Na(THF)_4$ → $Na(THF)_3$–$Na(THF)_3$ transitions and 16 ± 7 ps and 38 ± 18 ps for the $Na(THF)_2$–$Na(THF)_4$ → $Na(THF)_3$–$Na(THF)_4$ and $Na(THF)_3$–$Na(THF)_4$ → $Na(THF)_2$–$Na(THF)_4$ chemical reactions.

To further support the concept that these conversions occur as chemical reactions, we performed an analysis of our data using transition state theory, similar to the method described in our previous work,[16] briefly outlined here. According to transition state theory, inverse rates, τ, can be predicted according to $\tau = \tau_0 \exp\left(\frac{\Delta A^\ddagger}{k_B T}\right)$, where $\Delta A^\ddagger$ is the free energy barrier height for the interconversion and τ_0 is an inverse attempt frequency. We took $\Delta A^\ddagger$ to be the barrier height between coordination states, extracted from main text Fig. 3. With τ_0 set to 0.05 ps, conversion times of 32 ps and 35 ps for the $Na(THF)_3$-$Na(THF)_3$ → $Na(THF)_3$-$Na(THF)_4$ and $Na(THF)_3$-$Na(THF)_4$ → $Na(THF)_3$-$Na(THF)_3$ transitions and 16 ps and 40 ps for the $Na(THF)_2$-$Na(THF)_4$ → $Na(THF)_3$-$Na(THF)_4$ and $Na(THF)_3$-$Na(THF)_4$ → $Na(THF)_2$-$Na(THF)_4$ chemical reactions. Presumably the free energy barriers to other coordination states are too high to enable access during equilibrium dynamics but could be explored using umbrella sampling.

Potential of Mean Force Calculations

All potential of mean force plots along the coordination number coordinate were calculated as the negative natural logarithm of the occurance probability of each state. First, we binned up the number of production run configurations in each state, assuming Poisson statistics such that the error was simply its square root of the number of counts in each bin. Next, we normalized the histogram results by dividing by the maximum bin

count. Finally, we generated the PMF free energy values, A, in $k_{\mathrm{B}}T$ by taking the negative natural logarithm of the normalized bin counts. The normalization ensured that the most probable state is plotted at 0 $k_{\mathrm{B}}T$. The free energy error was propagated according to $\sigma = \pm\frac{\sqrt{\mathrm{bincount}}/\mathrm{maxbincount}}{\mathrm{bincount}/\mathrm{maxbincount}}$. Because the number of configurations in each Na_2 coordination state accessed at equilibrium in THF were similar, we did not need to use umbrella sampling to improve statistics (the relative population values for the $Na(THF)_3$-$Na(THF)_3$, $Na(THF)_2$-$Na(THF)_4$, and $Na(THF)_3$-$Na(THF)_4$ were 50:17:54 respectively). We also performed a similar analysis with bins along a coordinate consisting of the Na^+–Na^+ for each solvated configuration state.

The results of this analysis for the Na_2 coordination state and bond length are shown in the Main Text Figs. 3 (coordination state) and 4 (bond length). The free energy values for Main Text Fig, 4 were converted to eV for better comparison between the results in liquid Ar and THF with the gas-phase potential energy surface. We also calculated PMFs for the dipole moment magnitudes, angles, and projections along the bond axis for each Na_2 condensed phase state to further reveal the differences between each of these unique coordination states, shown in Supplementary Figs. 1–3 below.

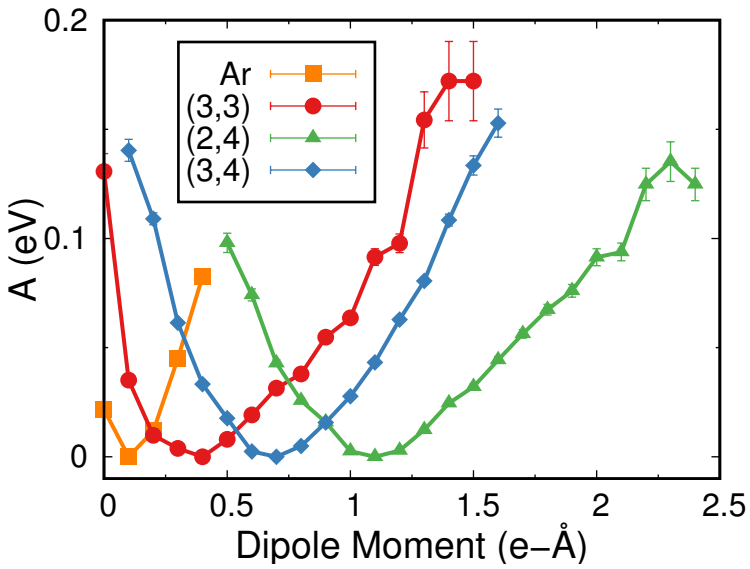

Supplementary Figure 1: PMF for the dipole moment magnitude.

Supplementary Figure 1 shows that the asymmetrically-coordinated solvation states in THF have, on average, higher dipole moments than symmetrically coordinated states, with the $Na(THF)_2$–$Na(THF)_4$ state (green curve) producing the largest average dipole moment of 1.1 *e*-Å. However, even the symmetrically coordinated $Na(THF)_3$–$Na(THF)_3$ state (red curve) has significant instantaneous dipole moments, on average around 0.4 e-Å (which is significantly larger than that seen in liquid Ar). However, even though the average dipole values induced in Na_2 in liquid Ar are small compared to those in liquid THF, the dipole moment magnitudes in liquid Ar are still significant compared to the gas phase.[11]

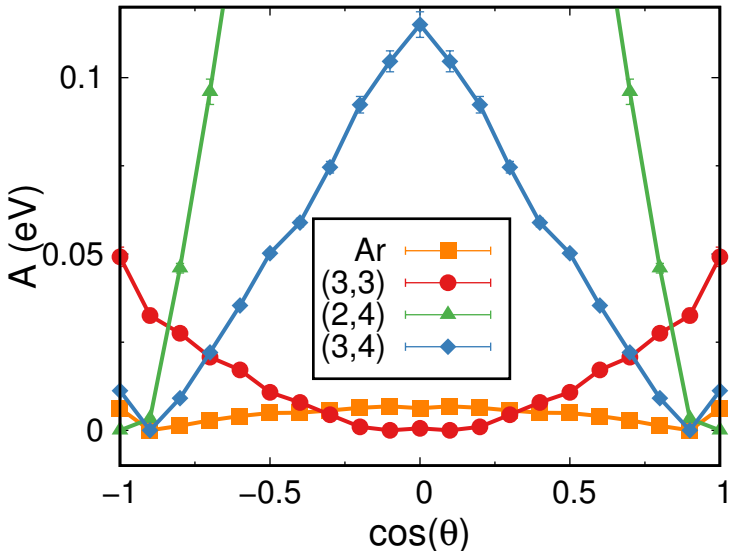

Supplementary Figure 2: PMF for the angle between the dipole moment vector and the bond axis. A value of $\cos(\theta) = 0$ means the dipole moment is oriented perpendicular to the bond axis while a value of ± 1 means the dipole moment is oriented along the bond axis.

Supplementary Figure 2 shows calculated PMFs of the angle the dipole moment makes with the Na_2 bond axis, revealing that in liquid Ar, the dipole moments are truly randomly oriented, with almost equal probability for the dipole to face in any direction. In liquid THF, however, we see two vastly different scenarios: asymmetrically-coordinated solvation states have dipole moments that prefer to point nearly directly along the bond axis while symmetrically-coordinated solvation states prefer to point nearly perpendicular to the bond axis, likely because the presence of equal numbers of coordinating solvent molecules on each Na atom make charge fluctuations along the bond axis less likely than those off-axis.

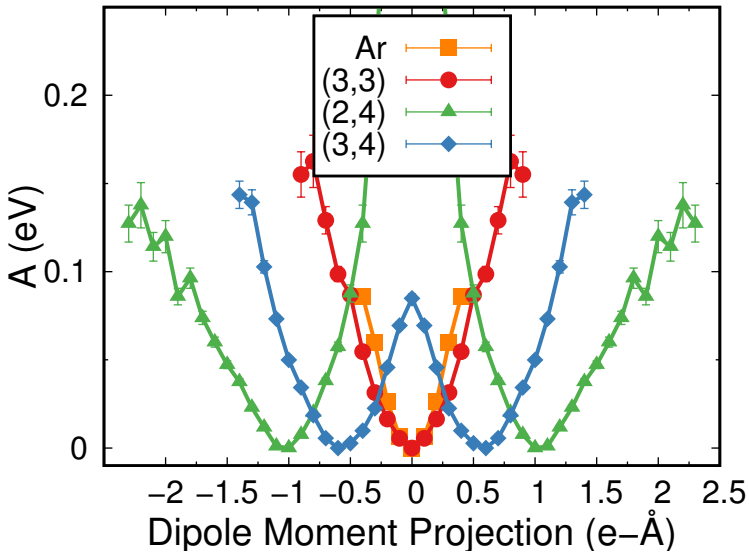

Supplementary Figure 3: PMF for the projection of the dipole moment vector onto the bond axis.

Perhaps most tellingly, Supplementary Figure 3 shows PMFs of the dipole moment projected along the bond axis, which reveal that asymmetrically coordinated Na_2 in THF have permanent dipole moments along the bond axis while symmetrically coordinated states and Na_2 in Ar have no permanent dipole moment, instead simply picking up instantaneous dipole moments around a zero average due to local solvent fluctuations.

Simulated Spectra Calculations

To produce calculated power and infrared (IR) spectra of Na_2, we first investigated the time dependence of the instantaneous bond velocity and dipole moment of Na_2 by calculating autocorrelation functions for each of these parameters, $C(t) = \langle X(t) \cdot X(0) \rangle$, where $X(t)$ is the bond velocity/dipole moment at time t. Since the Na_2 molecule interconverts between multiple stable coordination states in liquid THF, we selected segments from the equilibrium trajectory where the Na_2 remained in one coordination state for several picoseconds and then averaged the autocorrelation functions for each unique coordination state to improve statistics. The corresponding power/IR spectra were determined as the Fourier transform of $C(t)$. Further details of these calculations can be found in Glover *et al.*[11]

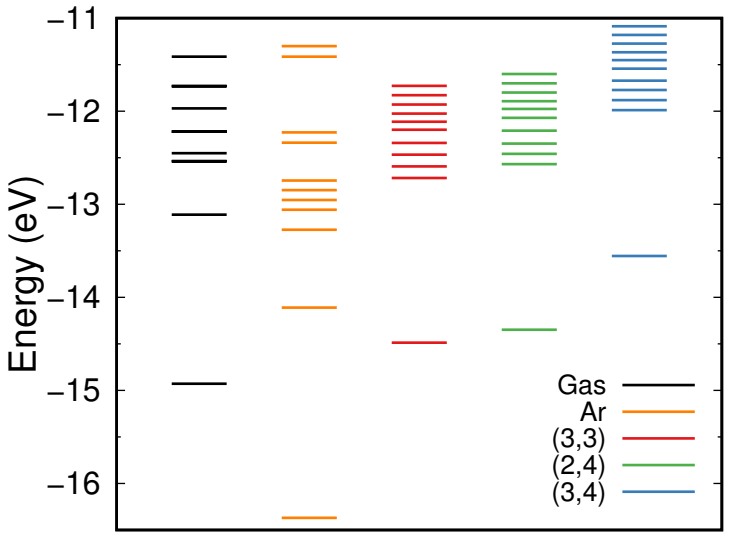

Supplementary Figure 4: Energy eigenvalues for the ground state and first ten excited states of Na_2 in the gas phase and condensed phase environments.

Our 2EFG method was used to calculate the eigenstates for the ground state and first ten electronic excited states for Na_2 in the gas phase, in liquid Ar, and in each equilibrium coordination state in liquid THF. Comparing the eigenvalues in these different environments, Supplementary Fig. 4 reveals the striking effects of the condensed phase on the electronic structure of Na_2. In Ar, the ground state is stabilized by almost 2 eV while the spacing between eigenstates is increased due to the compression of the Na_2 valence electrons by the cage of Ar atoms. The ground state of Na_2 in all THF environments is destabilized with an increasing destabilization associated with increased coordination. Interestingly, the most stable Na_2 coordination state in THF (that with the lowest free energy), $Na(THF)_3$–$Na(THF)_4$, is the most electronically destabilized of the equilibrium states. This indicates that the free energetic gain acquired from the addition of one more coordinating THF (relative to $Na(THF)_3$–$Na(THF)_3$ and $Na(THF)_2$–$Na(THF)_4$) is sufficient to offset the electronic destabilization. Also of note is the fact that the $Na(THF)_3$–$Na(THF)_3$ and $Na(THF)_2$–$Na(THF)_4$ species have similar degrees of electronic destabilization and eigenvalue spacings. This explains why these two coordination states have very similar absorption spectra, as seen in Fig 5c of the main text.

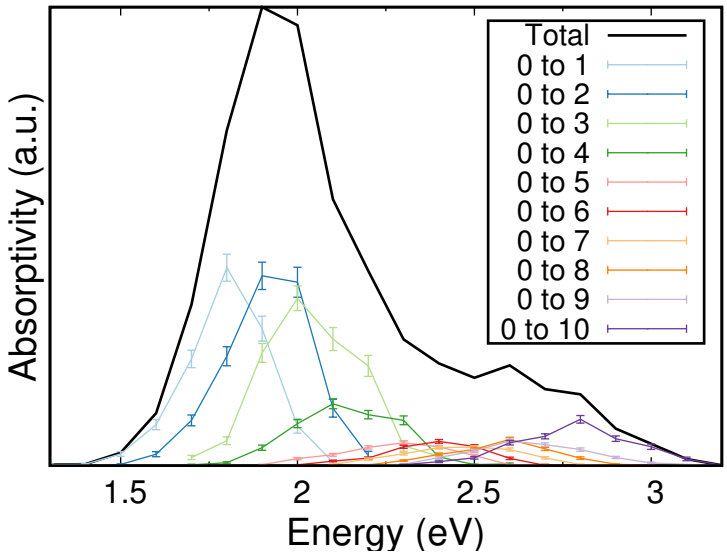

Supplementary Figure 5: Absorbance spectrum of the $Na(THF)_3$-$Na(THF)_3$ coordination state showing the individual inhomogeneous contributions from the transitions from the ground state to each of the first ten excited states.

By determining the transition dipoles between the Na_2 valence electronic ground state and the first ten excited states, we calculated the absorption spectrum of each coordination state in the inhomogeneous broadening limit according to

$$I(E) \propto \left\langle \sum_j |\boldsymbol{\mu}_{0j}|^2 \Delta E_{0,j} \delta\left(E - \Delta E_{0j}\right) \right\rangle \tag{7}$$

where j runs over the excited states and $\Delta E_{0,j}$ and $\boldsymbol{\mu}_{0j}$ are respectively the energy difference and transition dipole between the ground and jth state.[2,16] We used a histogram bin width of 0.1 eV. An example of the individual contributions of the transition from the ground to each excited state to the overall absorption spectrum is given in Supplementary Fig. 5 for the $Na(THF)_3$-$Na(THF)_3$ coordination state.

Verification of Results with Density Functional Theory (DFT) Calculations

As a means of verifing the accuracy of our theoretical model (chosen pseudopotentials, CISD grid solver, etc.), we performed DFT calculations on representative coordination states

(and some transition states) of Na_2 in THF. First, we selected configurations of each coordination state at the minimum of its potential of mean force – i.e., its equilibrium bond distance. Because our model uses planar THF with CH_2 groups treated as a united atom, we first explicitly added the hydrogen atoms and then optimized the overall structure with DFT using the B3LYP functional with the 6-31+G* basis set as implemented in QCHEM 5.0. With B3LYP, the optimized structures had Na–Na bond lengths of 3.68, 3.57, and 3.81 Å for the $Na(THF)_2$–$Na(THF)_4$, $Na(THF)_3$–$Na(THF)_3$, and $Na(THF)_3$–$Na(THF)_4$ states, respectively. The Na–THF oxygen site dative bond length were, on average, 2.45 ± 0.03 Å. We then performed single-point calculations of each geometrically-relaxed coordination state to determine the relative energies using the range-separated hybrid ωB97M-V functional, which includes non-local correlation. To compare the energies of coordination states with different total numbers of THF molecules (e.g., (3,4) vs. (3,3) and (2,4), we added or subtracted the energy of an isolated THF molecule calculated at the same level of theory. The ωB97M-V calculations predicted that, in agreement with our MQC calculations, the $Na(THF)_3$–$Na(THF)_4$ was the most stable coordination state, with the $Na(THF)_3$–$Na(THF)_3$ being next stable (110 meV or $\sim$4.3 k_BT higher) and $Na(THF)_2$-$Na(THF)_4$ being least stable (160 meV or $\sim$6.2 k_BT higher). We then tested the barrier heights, approximated as the energy needed to pull one THF from $Na(THF)_3$–$Na(THF)_4$ to form either $Na(THF)_3$–$Na(THF)_3$ or $Na(THF)_2$–$Na(THF)_4$. These values were 454 meV ($\sim$17.7 k_BT) for the $Na(THF)_3$–$Na(THF)_3$ $\rightarrow$ $Na(THF)_3$–$Na(THF)_4$ transition and 291 meV ($\sim$11.4 k_BT) for the $Na(THF)_2$–$Na(THF)_4$ $\rightarrow$ $Na(THF)_3$–$Na(THF)_4$ transition.

Interestingly, if B3LYP was used instead of ωB97M-V, $Na(THF)_3$–$Na(THF)_3$ was predicted to be the most stable state, $Na(THF)_3$-$Na(THF)_4$ next most stable (81 meV or $\sim$3.2 k_BT higher) and $Na(THF)_2$–$Na(THF)_4$ the least stable (121 meV or $\sim$4.7 k_BT higher). The calculated energy barriers were 356 meV ($\sim$13.9 k_BT) for the $Na(THF)_3$–$Na(THF)_3$ $\rightarrow$ $Na(THF)_3$–$Na(THF)_4$ transition and 269 meV ($\sim$10.5 k_BT) for the $Na(THF)_2$–$Na(THF)_4$ $\rightarrow$ $Na(THF)_3$–$Na(THF)_4$ transition. This shows that the assumptions and details of the DFT functional chosen has an effect on the prediction of the most stable coordination state and the relative energies of each state. However, the more accurate ωB97M-V shows better agreement with our MQC model.

Of course, our MQC model includes the presence of other THFs that help to solvate the different coordination states. To account for this, we ran the ωB97M-V, calculations with implicit THF solvent using a PCM dielectric continuum with THF's dielectric constant of 7.6. With the implicit solvent, all of the coordination-state energies stabilized slightly and the energy barriers lowered relative to the energies of the coordination states. Again, $Na(THF)_3$–$Na(THF)_4$ was the most stable species, followed by $Na(THF)_3$–$Na(THF)_3$ at just 47 meV ($\sim$1.8 k_BT) and $Na(THF)_2$–$Na(THF)_4$ at 93 meV ($\sim$3.6 k_BT). The energy barriers were reduced to 218 meV ($\sim$8.5 k_BT) for the $Na(THF)_3$–$Na(THF)_3 \rightarrow Na(THF)_3$–$Na(THF)_4$ transition and 201 meV ($\sim$7.8 k_BT) for the $Na(THF)_2$–$Na(THF)_4 \rightarrow Na(THF)_3$–$Na(THF)_4$ transition. These values are all within one-to-two k_BT of what we calculated in the MQC simulations, and given the accuracy of DFT, we consider the agreement to be excellent. The energy values for the latter calculations including implicit solvent are what is plotted as the black asterisks in Figs. 3b and c of the main text.

Representative Snapshots of Na_2 in Liquid Tetrahydrofuran

Figures 1b and c in the main text show representative snapshots of the simulations of Na_2 in liquid Ar and THF (in the (3,4) coordination state), respectively. Additional simulation snapshots and discussion are provided here to give a more comprehensive picture of the distortion of the Na_2 valence electron cloud for each coordination state. The Na^+ cores are plotted as black spheres (scaled to their ionic radius) while the valence electrons' density is represented as a transparent blue surface with a blue wire mesh coating enclosing 90% of the charge density. THF molecules are plotted as light-blue sticks with red oxygen atoms. The dative bonds between Na^+ and THF oxygen sites within 3.5 Å are drawn with thin black lines.

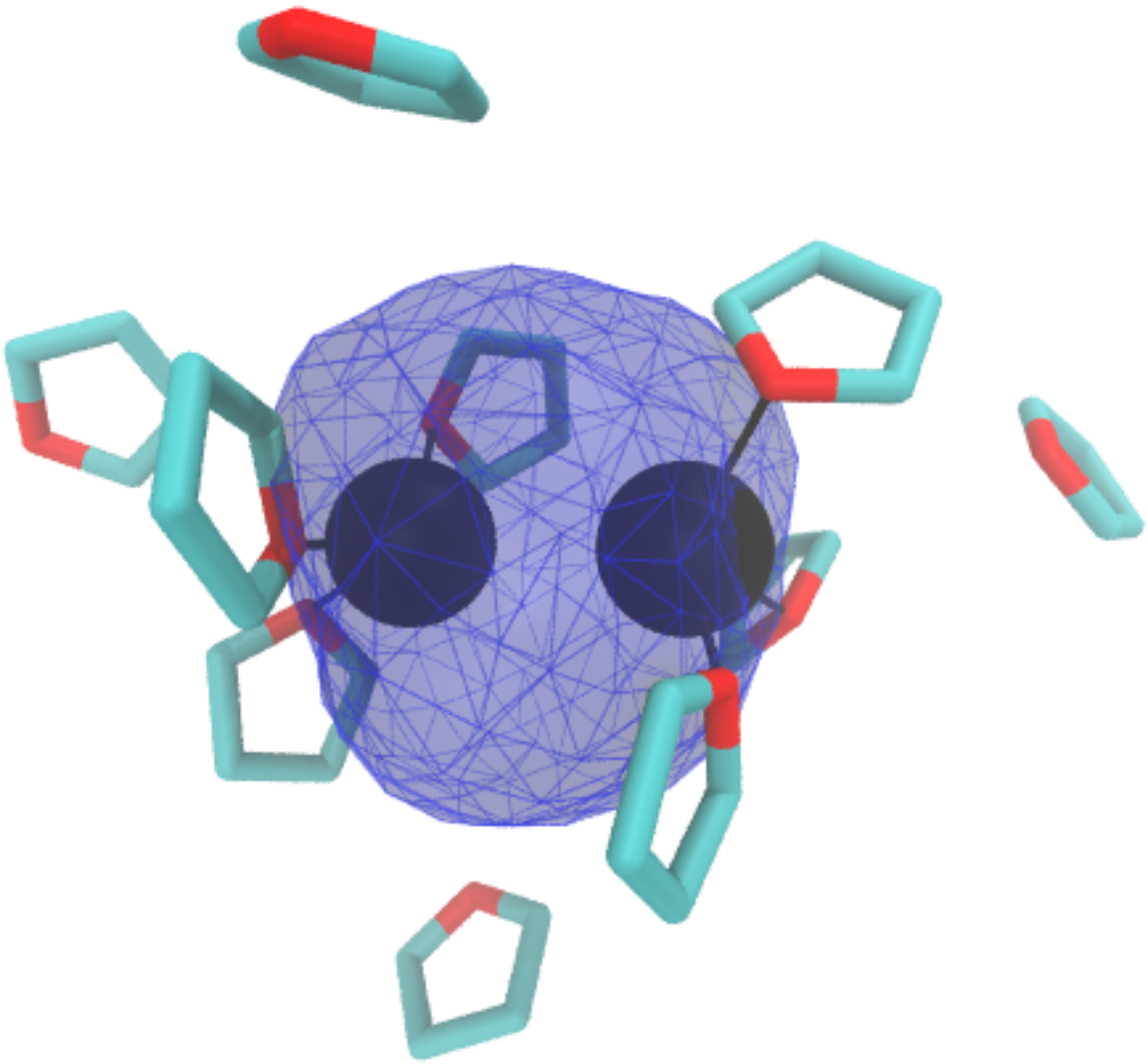

Supplementary Figure 6: A representative snapshot of the $Na(THF)_3$–$Na(THF)_3$ coordination state with bond length of 3.48 Å. Because the $Na(THF)_3$–$Na(THF)_3$ is a symmetrically coordinated state, the electron density is not shoved dramatically more toward either Na^+ cation core. Instead, the electron density primarily spills above and below the bonding axis, and although instantaneous dipole moments along the bond axis can occur due to interactions from uncoordinated solvent molecules, the average dipole moment is zero.

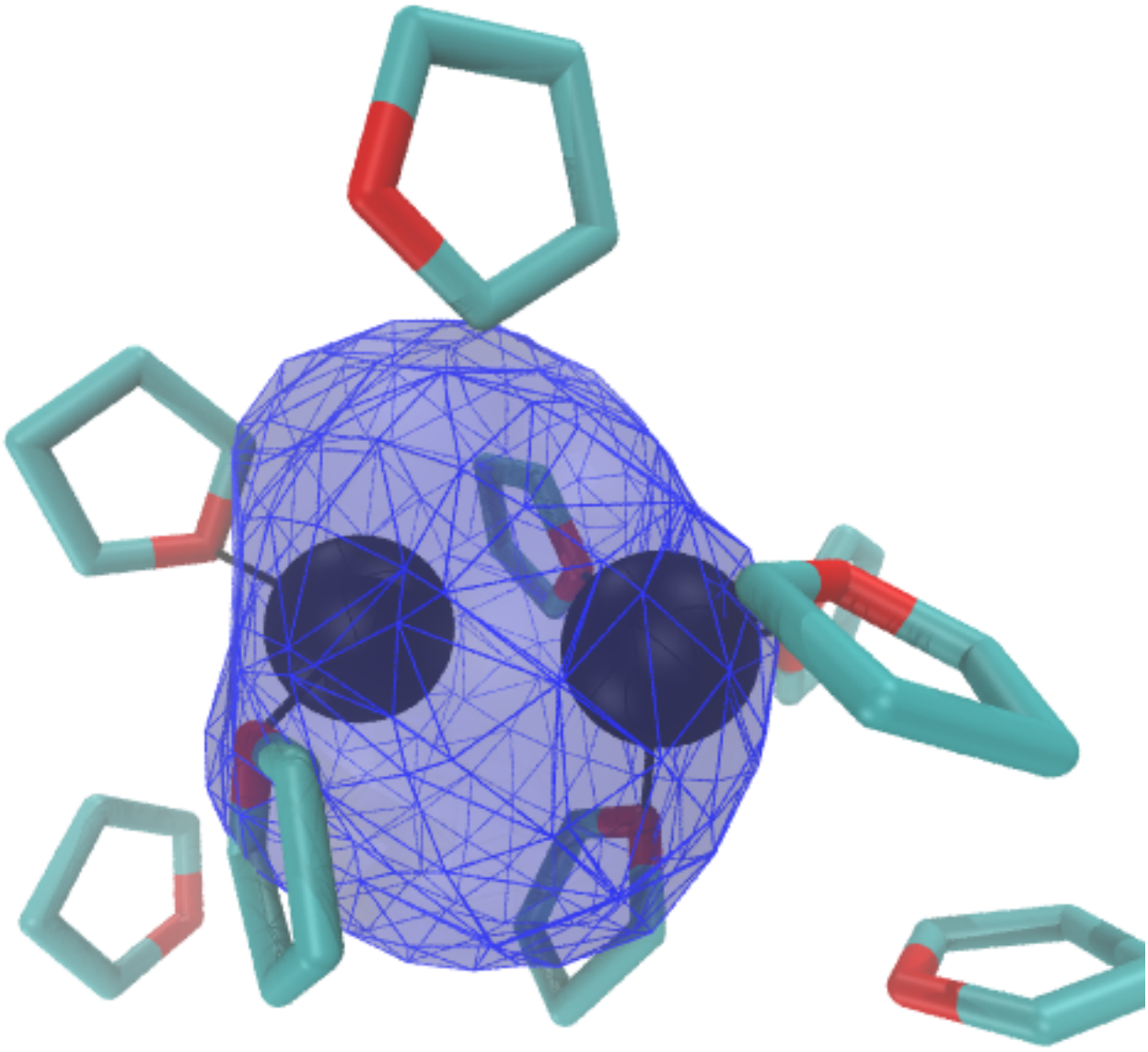

Supplementary Figure 7: A representative snapshot of the $Na(THF)_2$–$Na(THF)_4$ coordination state with bond length of 3.65 Å. Two THF molecules coordinate the left Na^+ core while four coordinate the right core. The electron density is highly distorted in this asymmetric coordination state, with more density pushed toward the left, away from the more highly-coordinated core, leading to a permanent average dipole moment. In addition, there is clearly still some distortion of the electron density around the less coordinated Na^+ as the two coordinating THF molecules need to push electron density aside to form their dative bonds to the core.

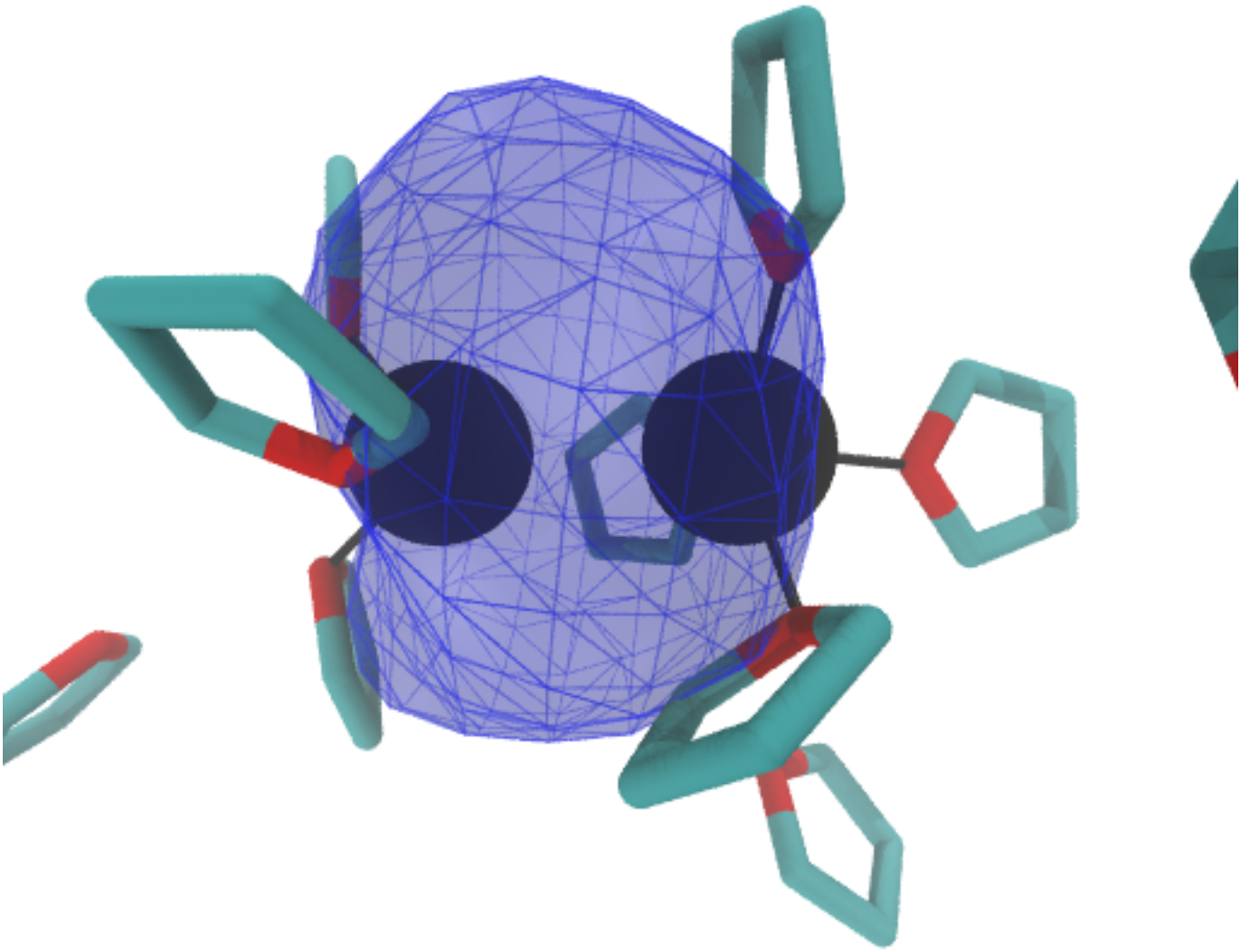

Supplementary Figure 8: A representative snapshot of the $Na(THF)_3$–$Na(THF)_4$ coordination state with bond length 3.70 Å. In this configuration, three THF molecules have formed dative bonds with the left-hand Na^+ cation core while four have formed dative bonds with the right-hand core. Due to the crowding of so many THF molecules around each core, the bonding electron density spills out significantly above and below the bonding axis. However, slightly more density shifts toward the less coordinated core to compensate for the extra crowding around the right-hand core, leading to a permanent dipole moment for the $Na(THF)_3$–$Na(THF)_4$ coordination state.

References

[1] Chandrasekhar, J., & Jorgensen, W. L. The nature of dilute-solutions of sodium-ion in water, methanol, and tetrahydrofuran. *J. Chem. Phys.* **77**, 5080-5089 (1982).

[2] Glover, W. J., Larsen, R. E., & Schwartz, B. J. The nature of sodium atoms/(Na^+-e^-) contact pairs in liquid tetrahydrofuran. *J. Phys. Chem. B.* **114**, 11535-11543 (2010).

[3] Allen, M. P. & Tildesley, D. J. *Computer Simulation of Liquids* (Oxford University Press, London, 1992).

[4] Steinhauser, O. Reaction field simulation of water. *Mol. Phys.* **45**, 335-348 (1982).

[5] Ahmadi, G. R., Almlöf, J., & Røeggen, I. The interaction potential for the $X^1\Sigma^+$ state of $ArNa^+$, $NeNa^+$ and $HeNa^+$. *Chem. Phys.* **199**, 33-52(1995).

[6] Gervais, B., et al. Simple DFT model of clusters embedded in rare gas matrix: Trapping sites and spectroscopic properties of Na embedded in Ar. *J. Chem. Phys.* **121**, 8466-8480 (2004).

[7] Phillips, J. C. & Kleinman, L. New method for calculating wave functions in crystals and molecules. *Phys. Rev.* **116**, 287-294 (1959).

[8] Larsen, R. E., Glover, W. J., & Schwartz, B. J., Does the hydrated electron occupy a cavity? *Science* **329**, 65-69 (2010).

[9] Smallwood, C. J., Larsen, R. E., Glover, W. G., & Schwartz, B. J. A computationally-efficient exact pseudopotential method. I. Analytic reformulation of the Philips-Kleinman theory. *J. Chem. Phys.* **125**, 1-8 (2006).

[10] Smallwood, C. J., Mejia, C. N., Glover, W. R., Larsen, R. E., & Schwartz, B. J. A computationally-efficient exact pseudopotential method. 2. Application to the molecular pseudopotential of an excess electron interacting with tetrahydrofuran (THF). *J. Chem. Phys.* **125**, 9681-9691 (2006).

[11] Glover, W. J., Larsen, R. E., & Schwartz, B. J. How does a solvent affect chemical bonds? Mixed quantum/classical simulations with a full CI Treatment of the bonding electrons. *J. Phys. Chem. Lett.* **1**, 165-169 (2010).

[12] Glover, W. J., Larsen, R. E., & Schwartz, B. J. The roles of electronic exchange and correlation in charge-transfer-to-solvent dynamics: Many-electron non-adiabatic mixed quantum/classical simulations of photoexcited sodium anions in the condensed phase. *J. Chem. Phys.* **129**, 1-20 (2008).

[13] Glover, W. J., Larsen, R. E., & Schwartz, B. J. First principles multi-electron mixed quantum/classical simulations in the condensed phase. I. An efficient fourier-grid method for solving the many-electron problem. *J. Chem. Phys.* **132**, 1-11 (2010).

[14] Lehoucq, R. B., Sorensen, D. C., & Yang, C. *ARPACK Users' Guide: Solution of Large-Scale Eigenvalue Problems with Implicitly Restarted Arnoldi Methods* (SIAM, Philadelphia, PA, 1998).

[15] Smit, B. Phase-diagrams of Lennard-Jones fluids. *J. Chem. Phys.* **96**, 8639-8640 (1992).

[16] Glover, W. J., Larsen, R. E., & Schwartz, B. J. Simulating the formation of sodium:electron tight-contact pairs: Watching the solvation of atoms in liquids one molecule at a time. *J. Phys. Chem. A* **115**, 5887-5894 (2011).